THE ASTROPHYSICAL JOURNAL, 406:158–171, 1993 March 20

AN EXPANDED SET OF BROWN DWARF AND VERY LOW MASS STAR MODELS

A. BURROWS,[1] W. B. HUBBARD,[2] D. SAUMON,[2] AND J. I. LUNINE[2]
Received 1992 August 12; accepted 1992 September 24

ABSTRACT

We present in this paper updated and improved theoretical models of brown dwarfs and late M dwarfs (VLMs). The evolution and characteristics of objects between 0.01 and 0.2 $M_\odot$ are exhaustively investigated and special emphasis is placed on their properties at early ages (10^6–10^8 yr). The dependence on the helium fraction, deuterium fraction, and metallicity of the masses, effective temperature and luminosities at the edge of the hydrogen main sequence are calculated. We derive luminosity functions for representative mass functions and compare our predictions to recent cluster data. We show that there are distinctive features in the theoretical luminosity functions that can serve as diagnostics of brown dwarf physics. A zero-metallicity model is presented as a bound to or approximation of a putative extreme halo population. This study is a continuation of that of Burrows, Hubbard, & Lunine (1989) and is meant to provide an expanded set of standard stellar models both just above and below the lower main-sequence edge for comparison with the new data in clusters, binaries, and in the field.

Subject headings: stars: evolution — stars: interiors — stars: low-mass, brown dwarfs

1. INTRODUCTION

Below the edge of the hydrogen-burning main sequence lies the realm of the brown dwarf. While these substellar objects are not massive enough to ignite hydrogen stably, they occupy what is in principle an extension of the M-dwarf stellar branch. Very low mass stars (VLMs, late M-dwarfs) and brown dwarfs share many features (Nelson, Rappaport, & Joss 1985). Apart from being very light ($0.01 \leq M \leq 0.3\ M_\odot$), their cool (effective temperature, $T_e < 3000$ K), high-density atmospheres are dominated by H_2 molecules, they are compact ($0.08 < R < 0.2\ R_\odot$), the Coulomb corrections to their equation of state (EOS) are significant, they emit predominantly in the red and infrared, and they are dim ($10^{-7} < L < 0.1\ L_\odot$). Dimness and the mass, age, and metallicity ambiguities of brown dwarf candidates woefully compromise the Galactic census of stars at and below the edge of the main sequence. Nevertheless, the observational situation has improved significantly in the last 5 years through the application of advanced infrared techniques. Surveys in the solar neighborhood (Henry & McCarthy 1990), in the field (for a review see Burrows & Liebert 1993), and in young stellar associations such as ρ Ophiuchi (Comeron et al. 1992), the Pleiades (Simons & Becklin 1992), and the Hyades (Leggett & Hawkins 1988; Bryja et al. 1992) are expanding the data base near and below the main-sequence cutoff. In order to meet the challenge of these new data and the profusion of new brown dwarf candidates, we present in this paper updated and extended theoretical models of objects between 0.01 and 0.2 $M_\odot$, from ages of 10^6 to 2×10^{10} yr. We investigate the dependence of brown and M-dwarf characteristics on helium (Y_α) and deuterium fraction (Y_d) and on metallicity (with Z = solar and $Z = 0$ atmospheres). Special emphasis is placed on theoretical predictions of the properties of young objects that, because they are bright, are selected for in searches. This paper should be viewed as a successor to Burrows, Hubbard, & Lunine (1989, hereafter BHL) and incorporates improved atmospheric and interior physics. However, we do not here explore the mixing-length and opacity prescription dependences as was done in BHL. Rather, we focus on a clean fiducial model with mixing-length parameter $\alpha = l_p/H = 1$. We present luminosity functions derived from our new models that exhibit distinctive observable features and compare the new theory with data from the recent cluster searches. Indeed, one of the rationales for the new study is that the searches for brown dwarfs are now focusing on clusters less than 10^8 yr in age. VLMs and brown dwarfs in this regime are characterized by large effective temperatures and large radii, outside the range considered in BHL. We have made changes in our treatment of the interiors and atmospheres to permit the modeling of these early phases. Furthermore, new pressure-induced opacities for hydrogen from Lenzuni, Chernoff, & Salpeter (1990) that are a significant departure from those of Patch (1971) are incorporated here. These new opacities are very significant for the $Z = 0$ models.

2. SHORT DESCRIPTION OF NEW MODEL PHYSICS

The atmospheric models, as described in Lunine et al. (1989), have been significantly modified for the present effort. In particular, to obtain a closed form for the temperature versus optical depth, we had used the standard Eddington approximation, $J = 3K$ throughout the atmosphere, where J is the mean intensity and K is the second moment of the radiation field. Such an approximation is valid for an atmosphere fully in radiative equilibrium, or for one in which the convection zone begins at large optical depth (and, hence, essentially is decoupled from the radiative zone).

For brown dwarfs and VLMs of high effective temperature (i.e., above 2500 K) and low surface gravity, we find that the top of the convection zone is at optical depths well below unity, invalidating the use of the Eddington approximation. Therefore, we explicitly solve the transfer equation to derive the temperature profile, though we retain the gray assumption, i.e., we use Rosseland mean opacities. The radiative transfer code employed is modified from that of Bergeron, Wesemael, & Fontaine (1990), which solves the transfer equation for a temperature-pressure profile using the Feautrier method. The resulting Eddington factors are used in the fully linearized

[1] Departments of Physics and Astronomy, University of Arizona, Tucson, AZ 85721.
[2] Department of Planetary Sciences, University of Arizona, Tucson, AZ 85721.

equations of radiative transfer, energy flux conservation, and hydrostatic equilibrium to produce temperature and pressure corrections to the guessed structure with the Rybicki solution. Converged models have $\Delta T/T \sim 10^{-5}$, $\Delta P/P \sim 10^{-4}$ and total flux conservation is achieved to better than one part in 10^4 for each layer of the model.

For the Population I metallicity models, the opacities used are as described in Lunine et al. (1989). Cloud (grain) opacity is included also as described in Lunine et al. (1989). Models in which cloud formation occurs are at low effective temperature (<2000 K) and then the Eddington approximation to the transfer equation was used so as to reduce computing time. Convection is handled in the models using the standard mixing-length treatment, with a mixing length set equal to the pressure scale height. The hydrogen equation of state for the atmosphere fully considers dissociation and ionization as described in BHL; this is required to correctly compute values of the molecular weight, adiabatic gradient, and specific heat throughout the atmosphere.

The models of BHL lie mostly at effective temperatures below 2500 K, for which we find the use of the Eddington approximation formalism acceptable. The surface boundary conditions based on our new gray atmosphere models represent a significant improvement over the work of BHL, D'Antona & Mazzitelli (1985), and Dorman, Nelson, & Chau (1989), for models with relatively high T_e relevant to the early phases of evolution and to the lower main sequence.

Figure 1 compares Population I gray atmosphere models computed with the Eddington approximation, as in BHL (*dashed lines*), and gray models obtained by solving the equation of radiative transfer (*solid lines*). The models are plotted on a background of entropy contours. This demonstrates how the $P(T)$ structure of the atmosphere becomes adiabatic in the convection zone. Molecular dissociation and ionization cause the stacking of isentropes near log $T \approx 3.4$ and log $T \approx 4.0$, respectively. The effect of convection in optically thin layers of the atmosphere on the entropy in the deep atmosphere is important for $T_e > 2500$ K. The difference between the full radiative and the Eddington approximation [prescribed $T(\tau)$] approaches is clear in Figure 1. Use of a prescribed $T(\tau)$ relationship has been standard in other recent models of VLMs and brown dwarfs, notably that of Stringfellow (1991), Nelson et al. (1993), and D'Antona & Mazzitelli (1985), which also focus on the high effective temperature models where shallow convection occurs. All these models are therefore subject to revision, since these atmospheres do not conserve flux (radiative plus convective) properly, and produce incorrect interior entropies per a given effective temperature and gravity.

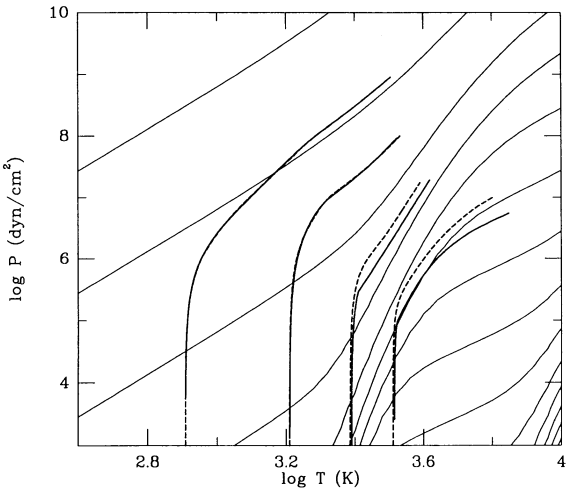

FIG. 1.—$P(T)$ profiles for solar metallicity gray atmospheres on a background of specific entropy contours (*thin lines*). The lowest contour line is in the upper left-hand corner with a value of $S = 6\,k_B$ per baryon and the spacing is $\Delta S = 2\,k_B$ per baryon. All models have log $g = 5.0$ and $T_e = 1000$, 2000, 3000, and 4000 K, from left to right. Models computed with the Eddington approximation are shown by dashed lines and models based on the solution of the radiative transfer are shown by solid lines.

3. RESULTS FROM THE STANDARD $Z = Z_\odot$ MODEL

To put in context the baseline models that we highlight in this paper, Table 1 and Figure 2 summarize the comparison of models with different helium fractions ($Y_\alpha = 0.22$, 0.25, 0.28) and either solar or zero metallicity. All of these models use $\alpha = l_p/H = 1.0$ and models B and G come from BHL. Table 1 contains the main-sequence edge mass (M_{edge}), and Figure 2 depicts luminosity-mass isochrones at 10^{10} yr. The dots in Figure 2 denote the main-sequence edge positions. As Table 1 demonstrates, M_{edge} is a decreasing function of Y_α and can be as low as 0.074 $M_\odot$ for $Z = Z_\odot$, though T_{edge} and L_{edge} are only weak functions of Y_α. However, as might be expected, the zero-metallicity models are very different, with M_{edge} from 0.094 to 0.098 $M_\odot$ and T_{edge} and L_{edge} at twice and 20–30 times, respectively, the $Z = Z_\odot$ values. Furthermore, the main-sequence edge, though precipitous for all models for late isochrones, is particularly so for the zero-metallicity cases. Note that M_{edge} is always below 0.1 $M_\odot$, even for the zero-metallicity models. This is in contrast to the higher value ($\sim$0.115 $M_\odot$) found in D'Antona (1987) and is a consequence of the new and higher pressure-induced H_2 opacities of Lenzuni et al. (1991). Figure 2 demonstrates that though changing Y_α merely slides the isochrone left or right, the large value of dL/dM in the VLM/BD transition region implies that at a given mass, say 0.08 $M_\odot$, the luminosity can vary by as much as a factor of 5. Thus, if a star is near M_{edge}, it is important to ascertain its composition before pronouncing it a brown dwarf.

Our standard model is a refinement of model G of BHL. We will call it model X. It has $Z = Z_\odot$, $Y_d = 2 \times 10^{-5}$, $Y_\alpha = 0.25$, and $\alpha = 1.0$ and incorporates the improvements cited in § 2. For this study, 45 mass models from 0.01 to 0.2 $M_\odot$ were evolved from 10^6 to 2×10^{10} yr. One million years was the time by which all transients due to initial conditions had died. Spherical symmetry was assumed along with no radiation or magnetic field.

Figure 3 portrays the evolution of the luminosity with time for objects from 0.01 $M_\odot$ ($\sim$10 Jupiter masses) to 0.2 $M_\odot$ with

TABLE 1

THE LOWER EDGE OF THE MAIN SEQUENCE

Model	Y_α	$Z/Z_\odot$	M_{edge}	T_{edge} (K)	$L_{edge}/L_\odot$
B	0.22	1	0.080	1770	6.59×10^{-5}
G	0.25	1	0.077	1760	6.21×10^{-5}
H	0.28	1	0.074	1740	5.72×10^{-5}
P[a]	0.22	0	0.098	3710	1.52×10^{-3}
Q[a]	0.25	0	0.094	3620	1.20×10^{-3}
X[b]	0.25	1	0.0767	1747	6.129×10^{-5}
Z[b]	0.25	0	0.094	3630	1.26×10^{-3}

[a] Low-resolution calculations for Y_α-dependence study alone.
[b] New, high-resolution models.

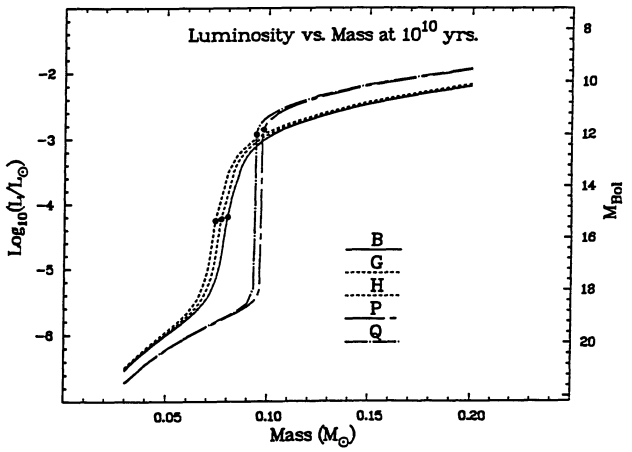

FIG. 2.—Luminosity (in solar units) vs. mass isochrones at 10^{10} yr for models B, G, H, P, and Q. The models are described in the text and in Table 1. The dots denote the edge of the hydrogen main sequence.

model X assumptions. In this figure, almost everything of relevance concerning the family of brown dwarfs and VLMs is reflected. From 10^6 to 10^7 yr, an object with mass greater than $\sim 0.015\ M_\odot$ burns primordial deuterium at roughly constant luminosity. For $Y_d = 2 \times 10^{-5}$, the "deuterium main-sequence" luminosities range between $\sim 3 \times 10^{-3}\ L_\odot$ (at $M = 0.02\ M_\odot$) and $0.3\ L_\odot$ (at $M = 0.2\ M_\odot$). During this phase, T_e and the radius (R) remain roughly constant, though in fact the ratio of the nuclear luminosity to the surface luminosity (L_n/L) peaks below 1.0, between 0.88 and 0.98. Lower mass stars emerge from the deuterium burning phase later and, though not shown in Figure 3, the highest mass stars (~ 0.15–$0.2\ M_\odot$) commence deuterium burning as early as $\sim 10^5$ yr.

As is clear from Figure 3, deuterium burning is crucially important below $\sim 10^7$ yr and maintains the luminosity above what would otherwise obtain without deuterium by as much as a factor of 5. Hence, for young clusters such as ρ Ophiuchus ($\sim 3 \times 10^6$ yr) and Taurus-Auriga ($\sim 10^6$ yr), deuterium burning cannot be ignored. If Y_d is increased to 5×10^{-5} (an extreme value to be sure), during deuterium burning the luminosities are larger by $\sim 50\%$ near the hydrogen main-sequence edge. In a sense, detailed future observations of young clusters might provide a crude handle on the primordial deuterium abundance, though this technique for ascertaining Y_d cannot be the preferred one.

After deuterium burning, the luminosities continue their decay. However, hydrogen burning proper commences near 2×10^8 yr for the more massive objects ($\geq 0.1\ M_\odot$) and near 10^9 yr for objects near $0.07\ M_\odot$. If the star has sufficient mass ($M > M_{edge}$), its luminosity stabilizes on the hydrogen main sequence. If not, though hydrogen burning may occur for a time, it aborts, and the object's luminosity continues its decay. The separation between these two branches, the VLMs and brown dwarfs, is clearly seen in the right of Figure 3. To resolve the edge, evolutionary calculations were performed in mass increments of at most $0.001\ M_\odot$ ($\sim 1 M_J$) (and right near the edge of $\sim 0.0001\ M_\odot$) in the transition region. The edge was found to be at $0.0767\ M_\odot$ for model X. Note that at an age of 2×10^{10} yr, the luminosity ranges an extraordinary six orders of magnitude for objects from 0.01 to $0.2\ M_\odot$.

Figures 4 and 5 depict the corresponding T_e and R evolutionary tracks for model X. Note that there is generally a peak in T_e, which occurs at earlier times for lower mass objects. As Figure 5 clearly shows, the radii are only roughly constant during deuterium burning, but are at values that are much larger than those to which they finally settle. Figures 6 and 7 show luminosity-mass and T_e-mass isochrones between 10^6 and 10^{10} yr. The bump at lower masses is due to deuterium burning. Table 2 provides the values of various relevant quantities for model X objects at various ages and recapitulates some of the data in Figures 3–7. These figures and the numbers in Table 2 summarize all of the important characteristics of

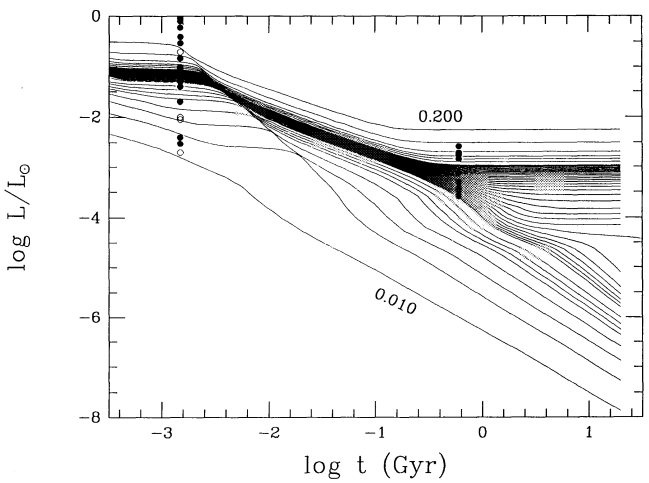

FIG. 3.—Luminosities as a function of time for the suite of Population I models (model X) presented here. Each curve is for a fixed mass from 0.01 (*lowest curve*) to $0.2\ M_\odot$ (*highest curve*). Starting with the lowest curve, masses are 0.010, 0.020, 0.030, 0.040, 0.050, 0.055, 0.060, and 0.065. The dense band of masses in the center of the figure spans the critical mass for hydrogen burning, and is at a mass interval of 0.001 from 0.070 through $0.100\ M_\odot$. A near-critical model at $0.076\ M_\odot$ is shown with evolution continued to $t > 30$ Gyr. The most massive models are computed for masses of 0.105, 0.110, 0115, 0.125, 0.150, and $0.200\ M_\odot$. The "ripple" which appears at $t \sim 10^{-3}$ to 10^{-2} Gyr is deuterium burning. Note the clear division into hydrogen burners and brown dwarfs at $t \sim 10$ Gyr. Solid dots on left represent low-luminosity ρ Oph objects from Table 4 of Comeron et al. (1992); open dots are objects from Table 5 of the same study, for which only two measured magnitudes are available. Solid dots on the right are low-luminosity Hyades objects from the study of Bryja et al. (1992).

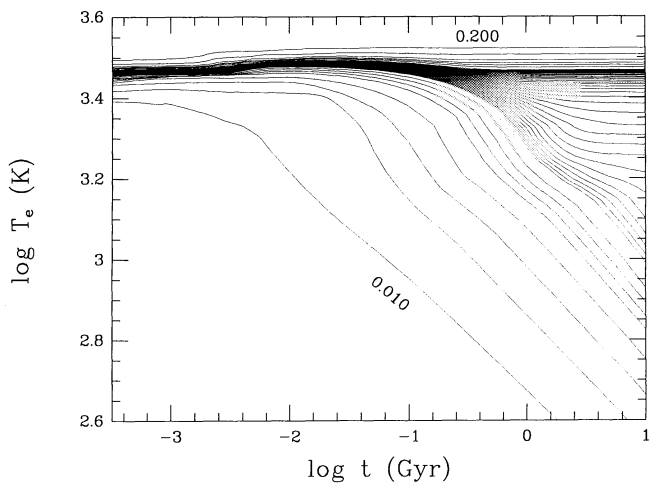

FIG. 4.—A plot similar to Fig. 3, but for effective temperature vs. time. The numbers 0.200 and 0.010 are in solar masses and denote the masses of the boundary models.

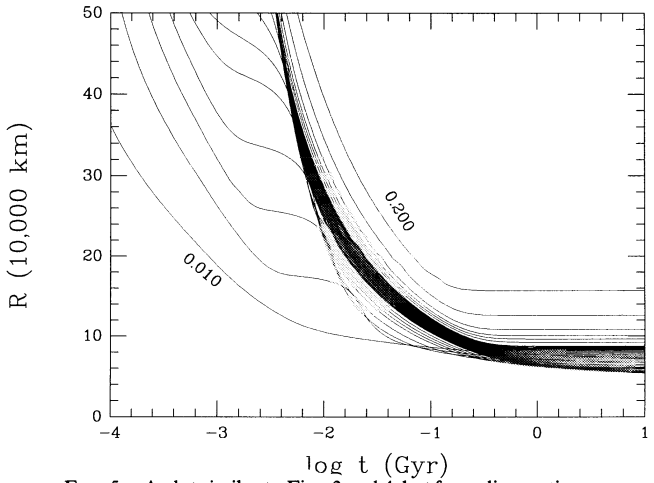

FIG. 5.—A plot similar to Figs. 3 and 4, but for radius vs. time

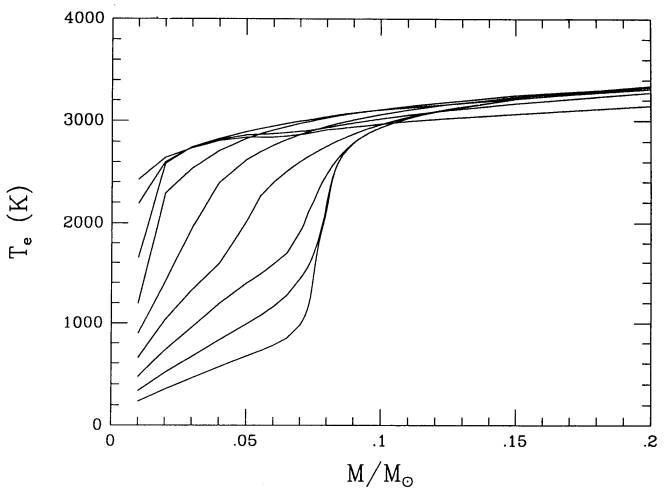

FIG. 7.—Isochrones of T_e vs. mass, Population I, at times from 10^{-3} Gyr (*top curve*) to 10 Gyr, in steps of 0.5 in log t.

standard model X for brown dwarfs and VLMs. They should prove useful for analyzing current and future observations for which an extended range of ages and masses is required.

To illustrate one of the uses of this set of figures, we have superposed on Figure 3 the recent data for ρ Ophiuchus from Comeron et al. (1992) and, for the Hyades, from Bryja et al. (1992). Comeron et al. report some seven substellar objects in the core of the ρ Oph stellar clouds, included among some 91 infrared sources. They use these results to derive a power-law mass function that extends into the brown dwarf region. In the next section, we present a more complete analysis of luminosity and mass functions for VLMs and brown dwarfs. However, it is interesting to note that unlike the results derived for VLMs in the Hyades by Hubbard, Burrows, & Lunine (1990), the Comeron study seems to penetrate into the brown dwarf mass range by virtue of the much higher luminosities of brown dwarfs in the very young ρ Oph association. As Figure 3 illustrates, despite the age ambiguity of the ρ Oph objects, if there are no significant errors in the extinction corrections and distance estimates, ρ Oph seems to be rich in brown dwarfs down to a mass of $\sim 0.01\ M_\odot$.

4. LUMINOSITY FUNCTIONS

A key comparison between theory and observation can be made with counts of brown dwarfs in a star cluster of known age. A principal and robust result of brown dwarf theory is that at sufficiently large age, the population of brown dwarfs moves steadily to lower luminosities and lower effective temperatures, while the population of objects stabilized on the lower main sequence remains constant. Thus, a gap eventually appears in the luminosity function at the critical mass.

We define the luminosity function $N(L, t)$ to be the number of stars per unit interval in $\log_{10}$ of luminosity L at time t. To convert our evolutionary sequences to N, we also assume the following IMF:

$$\xi(M)dM = CM^{-\alpha}dM\ . \qquad (1)$$

We have taken $\alpha = 0$ in the low-mass range of interest here (Hubbard et al. 1990). However, as we discuss below, there is some evidence that larger values of α apply in the mass range associated with BD's.

Results from some of our calculations are presented in Figures 8–14. Figure 8 shows the evolution of brown dwarf

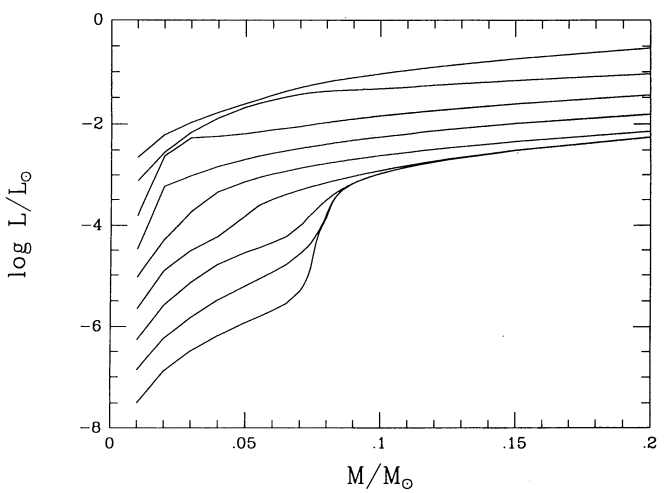

FIG. 6.—Isochrones of luminosity vs. mass, for Population I, at times from 10^{-3} Gyr (*top curve*) to 10 Gyr, in steps of 0.5 in log t.

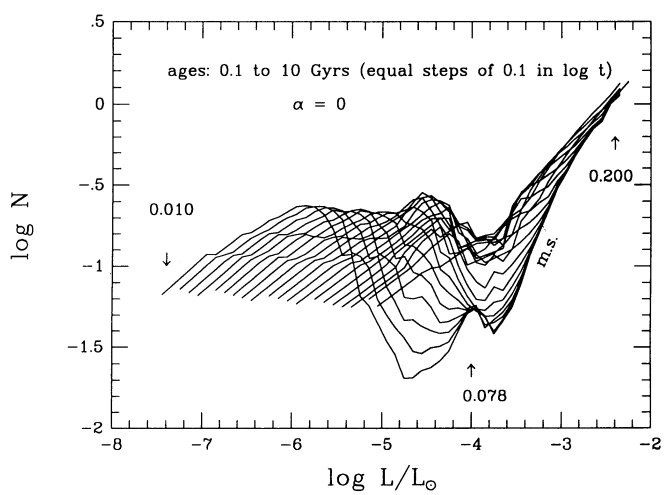

FIG. 8.—Isochrones of luminosity functions for Population I, at times from 10^{-1} Gyr (*top curve*) to 10 Gyr, in steps of 0.1 in log t, for $\alpha = 0$.

TABLE 2

MODEL X

$M/M_\odot$	Age	T_e	$L/L_\odot$	R	T_c	ρ_c	S	L_n/L
	10^9 yrs	K		10^9 cm	10^6 K	g/cm^3	k_B/baryon	
0.200	0.003	3273.	9.714E-02	67.41	1.639	1.9	16.70	0.000
	0.070	3340.	9.095E-03	19.81	4.949	67.1	13.66	0.088
	0.600	3331.	5.653E-03	15.70	6.041	135.4	13.05	1.000
0.150	0.003	3166.	7.332E-02	62.61	1.332	1.7	16.32	0.000
	0.070	3238.	5.865E-03	16.93	4.201	80.2	13.02	0.047
	0.600	3212.	3.143E-03	12.60	5.344	194.3	12.20	1.000
0.125	0.003	3103.	6.257E-02	60.20	1.165	1.6	16.09	0.000
	0.070	3170.	4.475E-03	15.42	3.776	87.7	12.62	0.027
	0.600	3111.	2.044E-03	10.82	4.897	253.0	11.59	0.997
	10.000	3111.	2.043E-03	10.82	4.898	253.3	11.59	1.000
0.115	0.003	3071.	5.759E-02	58.95	1.099	1.6	15.99	0.000
	0.070	3140.	3.964E-03	14.80	3.603	90.7	12.44	0.021
	0.600	3058.	1.649E-03	10.06	4.699	287.8	11.30	0.993
	10.000	3058.	1.647E-03	10.05	4.702	288.6	11.30	1.000
0.110	0.003	3054.	5.438E-02	57.94	1.071	1.6	15.93	0.000
	0.070	3122.	3.684E-03	14.43	3.458	94.9	12.34	0.019
	0.600	3026.	1.453E-03	9.65	4.492	315.4	11.13	0.990
	10.000	3025.	1.449E-03	9.64	4.495	316.8	11.13	1.000
0.105	0.003	3035.	5.281E-02	57.80	1.030	1.5	15.89	0.000
	0.070	3103.	3.452E-03	14.14	3.382	95.1	12.24	0.015
	0.600	2987.	1.267E-03	9.24	4.406	338.9	10.95	0.976
	10.000	2986.	1.258E-03	9.22	4.412	341.7	10.94	1.000
0.100	0.003	3016.	5.131E-02	57.70	0.988	1.5	15.85	0.000
	0.070	3082.	3.200E-03	13.80	3.310	96.2	12.14	0.013
	0.600	2941.	1.080E-03	8.81	4.306	368.7	10.74	0.959
	10.000	2938.	1.065E-03	8.76	4.314	374.5	10.72	1.000
0.095	0.003	2996.	5.000E-02	57.72	0.946	1.4	15.82	0.013
	0.070	3060.	2.959E-03	13.46	3.133	99.9	12.02	0.011
	0.600	2884.	9.026E-04	8.37	4.013	412.0	10.51	0.917
	10.000	2876.	8.730E-04	8.28	4.022	426.1	10.47	1.000
0.090	0.003	2975.	4.867E-02	57.76	0.904	1.3	15.78	0.091
	0.070	3035.	2.721E-03	13.12	3.053	101.0	11.90	0.009
	0.600	2812.	7.331E-04	7.93	3.852	453.4	10.25	0.838
	10.000	2788.	6.729E-04	7.73	3.854	489.3	10.15	1.000
0.088	0.003	2966.	4.812E-02	57.78	0.886	1.3	15.77	0.149
	0.070	3025.	2.628E-03	12.98	3.001	101.8	11.85	0.008
	0.600	2777.	6.661E-04	7.75	3.744	473.9	10.14	0.788
	10.000	2736.	5.834E-04	7.47	3.732	528.6	9.99	1.000
0.086	0.003	2957.	4.744E-02	57.71	0.870	1.3	15.75	0.216
	0.070	3015.	2.535E-03	12.84	2.920	103.5	11.80	0.007
	0.600	2739.	6.039E-04	7.59	3.580	495.9	10.02	0.731
	10.000	2674.	4.932E-04	7.20	3.536	580.0	9.80	1.000
0.084	0.003	2948.	4.668E-02	57.60	0.854	1.3	15.73	0.288
	0.070	3004.	2.443E-03	12.69	2.863	104.6	11.75	0.006
	0.600	2699.	5.460E-04	7.43	3.449	515.2	9.91	0.666
	10.000	2583.	3.935E-04	6.89	3.344	646.1	9.57	1.000
0.082	0.003	2939.	4.583E-02	57.43	0.840	1.3	15.70	0.361
	0.070	2992.	2.353E-03	12.55	2.832	104.9	11.69	0.006
	0.600	2656.	4.921E-04	7.29	3.356	530.7	9.80	0.591
	10.000	2426.	2.711E-04	6.48	3.112	750.9	9.24	1.000
0.080	0.003	2930.	4.491E-02	57.19	0.826	1.2	15.68	0.432
	0.070	2981.	2.263E-03	12.41	2.793	105.4	11.64	0.005
	0.600	2608.	4.402E-04	7.15	3.246	545.8	9.68	0.511
	10.000	2143.	1.471E-04	6.12	2.796	865.0	8.88	1.000
0.078	0.003	2921.	4.389E-02	56.90	0.813	1.2	15.65	0.498
	0.070	2968.	2.174E-03	12.26	2.772	105.4	11.58	0.004
	0.600	2557.	3.928E-04	7.03	3.165	556.1	9.57	0.431
	10.000	1920.	9.224E-05	6.04	2.668	873.7	8.75	1.000
0.076	0.003	2913.	4.270E-02	56.45	0.800	1.2	15.61	0.555
	0.070	2955.	2.087E-03	12.12	2.658	107.8	11.52	0.004
	0.600	2502.	3.493E-04	6.92	2.927	572.2	9.46	0.352
	10.000	1638.	4.603E-05	5.86	2.297	932.8	8.49	0.967
0.074	0.003	2905.	4.136E-02	55.86	0.788	1.2	15.57	0.603
	0.070	2942.	2.005E-03	11.99	2.591	108.7	11.47	0.003
	0.600	2448.	3.114E-04	6.82	2.772	579.7	9.36	0.280
	10.000	1263.	1.433E-05	5.50	1.728	1094.0	7.89	0.540

TABLE 2—*Continued*

$M/M_\odot$	Age	T_e	$L/L_\odot$	R	T_c	ρ_c	S	L_n/L
	10^9 yrs	K		10^9 cm	10^6 K	g/cm^3	k_B/baryon	
0.072	0.003	2897.	3.990E-02	55.13	0.776	1.2	15.52	0.642
	0.070	2928.	1.915E-03	11.83	2.561	109.0	11.40	0.003
	0.600	2392.	2.774E-04	6.74	2.676	580.1	9.27	0.220
	10.000	1081.	7.442E-06	5.41	1.516	1109.0	7.64	0.330
0.070	0.003	2893.	3.810E-02	54.03	0.766	1.3	15.47	0.664
	0.070	2914.	1.830E-03	11.67	2.520	109.8	11.35	0.003
	0.600	2331.	2.461E-04	6.69	2.567	575.0	9.19	0.167
	10.000	980.	4.979E-06	5.38	1.374	1090.0	7.51	0.195
0.065	0.003	2883.	3.350E-02	51.03	0.746	1.4	15.29	0.730
	0.070	2874.	1.621E-03	11.30	2.348	113.0	11.19	0.002
	0.600	2108.	1.588E-04	6.57	2.206	563.5	8.99	0.084
	10.000	852.	2.873E-06	5.42	1.122	987.8	7.35	0.056
0.060	0.003	2874.	2.917E-02	47.91	0.725	1.5	15.09	0.811
	0.070	2827.	1.418E-03	10.92	2.193	114.4	11.01	0.001
	0.600	1894.	1.027E-04	6.54	1.936	521.7	8.85	0.039
	10.000	781.	2.092E-06	5.49	0.977	866.9	7.26	0.016
0.055	0.003	2869.	2.488E-02	44.41	0.706	1.7	14.85	0.865
	0.070	2773.	1.223E-03	10.54	2.019	115.8	10.82	0.001
	0.600	1717.	6.985E-05	6.57	1.685	468.9	8.74	0.016
	10.000	723.	1.589E-06	5.58	0.842	749.2	7.20	0.004
0.050	0.003	2865.	2.086E-02	40.77	0.686	1.9	14.58	0.895
	0.070	2706.	1.031E-03	10.16	1.827	116.9	10.61	0.000
	0.600	1581.	5.111E-05	6.62	1.449	412.4	8.64	0.005
	10.000	669.	1.210E-06	5.69	0.712	637.3	7.15	0.001
0.040	0.003	2819.	1.310E-02	33.37	0.643	2.6	13.93	0.930
	0.070	2523.	6.710E-04	9.43	1.434	114.1	10.14	0.000
	0.600	1364.	2.965E-05	6.78	1.051	300.1	8.44	0.000
	10.000	565.	6.716E-07	5.94	0.509	437.3	7.03	0.000
0.030	0.003	2750.	7.057E-03	25.74	0.598	4.1	13.06	0.937
	0.070	2197.	3.371E-04	8.81	0.997	101.2	9.58	0.000
	0.600	1125.	1.459E-05	6.99	0.697	198.1	8.21	0.000
	10.000	460.	3.275E-07	6.26	0.349	271.1	6.90	0.000
0.020	0.003	2602.	2.952E-03	18.60	0.515	6.9	11.90	0.440
	0.070	1598.	9.270E-05	8.73	0.584	65.9	9.15	0.000
	0.600	848.	5.188E-06	7.33	0.397	108.8	7.95	0.000
	10.000	353.	1.287E-07	6.66	0.203	141.7	6.69	0.000
0.010	0.003	2198.	7.990E-04	13.56	0.312	8.0	10.57	0.001
	0.070	982.	1.347E-05	8.83	0.249	28.6	8.62	0.008
	0.600	546.	1.015E-06	7.84	0.174	39.7	7.67	0.001
	10.000	239.	3.141E-08	7.21	0.092	49.5	6.48	0.000

luminosity functions for relatively advanced ages, beginning at 0.1 Gyr. In addition to the previously described gap below the critical mass, two other features of this plot merit attention. At intermediate ages, a transient maximum in the luminosity function appears at $\log_{10} L/L_\odot \approx -4.5$; this maximum corresponds to effective temperatures $T_e \approx 1500$ K and is associated with the maximum effect of grain formation in brown dwarf atmospheres (Lunine et al. 1989). As the population of brown dwarfs evolves to even lower temperatures, where silicate grains move into the adiabatic region, this maximum disappears.

The other noteworthy feature in Figure 8 is a curious plateau in the luminosity function at $\log_{10} L/L_\odot \approx -3.8$ at the most advanced times (~ 10 Gyr). This plateau represents the very end of the main sequence, which extends down to $M = 0.078\ M_\odot$, and is caused by a fairly abrupt change in the steady state log L versus log M slope at mass $M = 0.081\ M_\odot$ (see Fig. 6). We thus predict that the very end of the main sequence should be characterized by a roughly constant luminosity function over a very limited range of masses.

Luminosity functions at earlier times are shown in Figures 9–11. A barely-resolved sequence of peaks is seen moving through the functions in Figures 9 and 10, for $\log t = -2$, -1.95, -1.9, and -1.85, at $\log_{10} L/L_\odot \approx -3$. These peaks are caused by early deuterium burning, which evidently has only a minor effect on luminosity functions for the initial deuterium abundance assumed here ($Y_d = 2 \times 10^{-5}$). At very early ages, ~ 0.001 Gyr, luminosity functions are essentially featureless, and maintain roughly constant slope while progressively moving to lower luminosities.

Figure 11 shows luminosity functions computed for specific cluster ages. For the three youngest clusters (Taurus, ρ Oph, Pleiades), the luminosity functions are given by essentially the same power law, while for the older clusters (Praesepe, Hyades), a peak associated with grain opacity effects begins to appear at very low luminosities ($\log_{10} L/L_\odot \approx -4.5$).

4.1. *Comparison with ρ Ophiuchi and Hyades Data*

Comeron et al. (1992), report some seven substellar objects in the cores of the ρ Oph stellar clouds. They use these results to derive a power-law exponent for the low-mass IMF in this region. Unlike results derived for low-mass objects in the

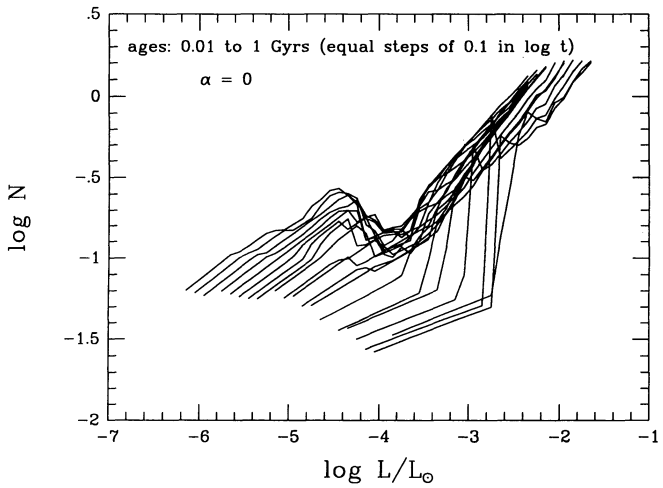

FIG. 9.—Isochrones of luminosity functions for Population I, at times from 10^{-2} Gyr (*top curve*) to 1 Gyr, in steps of 0.1 in log t, for $\alpha = 0$.

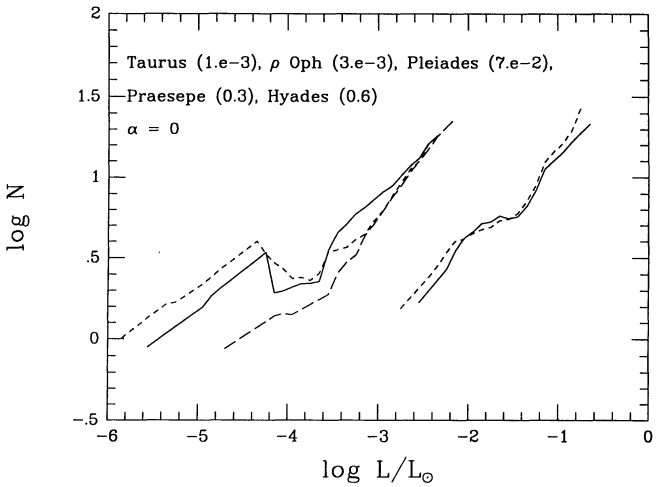

FIG. 11.—Isochrones of luminosity functions for Population I, at times corresponding to age of Taurus association (0.001 Gyr; *solid curve*), ρ Oph (0.003 Gyr, *short dashed curve*), Pleiades (0.07 Gyr, *long dashed curve*), Praesepe (0.3 Gyr, *solid curve*), and Hyades (0.6 Gyr, *short dashed curve*), assuming $\alpha = 0$.

Hyades by Hubbard et al. (1990), the Comeron study seems to penetrate significantly into the brown dwarf mass range by virtue of much higher luminosities of brown dwarfs in the very young ρ Oph association.

Because the maximum age of objects in ρ Oph is only 3×10^6 yr, and because star formation appears to be continuing at present, we use a mean age of 1.5×10^6 yr. The relevant data points (with error bars) from Comeron et al. are shown in Figure 12*a*. Clearly the best-fit model for the Hyades, with $\alpha = 0$, does *not* fit ρ Oph. Comeron et al. infer a best-fit value $\alpha = 1.14$ on the basis of the brown dwarf models of D'Antona & Mazzitelli (1985) and the entire ρ Oph luminosity function, which extends to $\log L/L_\odot = 2.5$. However, as Figure 12*a* shows, when we restrict the luminosity function to the range spanned by our VLM and brown dwarf models, an even steeper IMF, possibly as steep as the Salpeter (1955) model, is indicated. We also note that the brown dwarfs in the ρ Oph association are deuterium burners; the shallow maximum in the luminosity function at $\log L/L_\odot \approx -1.2$ is produced by deuterium burning.

We compare our theory with a much older cluster, the Hyades, in Figure 12*b*. Unlike Figure 12*a*, where the units of N (and hence the zero point of $\log_{10} N$) are arbitrary, in Figure 12*b* we plot the actual number of objects per interval of 0.3 in $\log_{10} L/L_\odot$. Data points shown with solid dots are the star counts of Leggett & Hawkins (1988, 1989). Data points marked with open circles are from the extended star counts of Leggett & Hawkins (1989), consisting of objects for which no proper motion was available and, hence, no assurance of Hyades membership was available. All of the above data were included in the study of Hubbard et al. (1990). Since that paper, an additional study by Bryja et al. (1992), has extended counts of faint Hyades members to lower luminosities, and has confirmed cluster membership by means of proper motions. The data of Bryja et al. are plotted as triangles in Figure 12*b*. We have used the same bins in $\log_{10} L/L_\odot$ as in Hubbard et al. (1990), and error bars represent the expected 1 σ fluctuations due to the finite number of stars in each bin. As is evident from Figure 12*b*, the new data of Bryja et al. are consistent with the extended list of Leggett & Hawkins. Even with the augmented data, there is considerable scatter in the points. If we attempt to fit the data with a single power-law IMF, the best-fit value would probably be in the range $\alpha = 0$–1.14. If both ρ Oph and the Hyades are required to have the same value of α, the best compromise appears to be $\alpha = 1.14$.

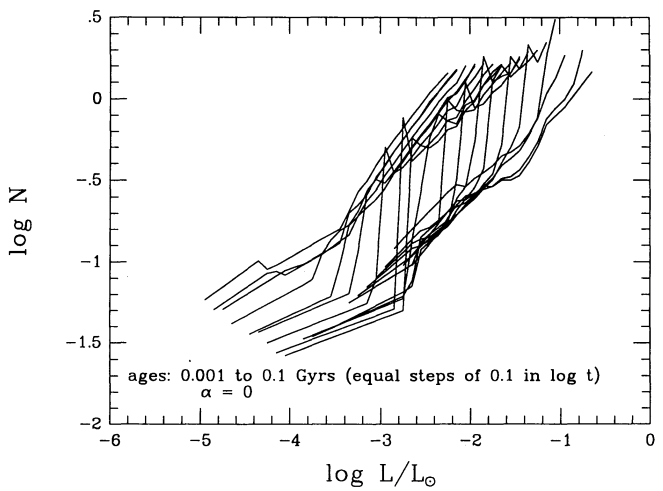

FIG. 10.—Isochrones of luminosity functions for Population I, at times from 10^{-3} Gyr (*top curve*) to 0.1 Gyr, in steps of 0.1 in log t, for $\alpha = 0$.

Considerable modification in the appearance of luminosity functions at later times occurs if we use the Comeron value of $\alpha = 1.14$. Figure 13 shows luminosity functions calculated with this index for several young clusters (here for ρ Oph we use an age of 3×10^6 yr), while Figure 14 shows the evolution of the luminosity functions for ages comparable to the age of the galaxy. (Fig. 14 is the same as Fig. 8, but for $\alpha = 1.14$.) As for $\alpha = 0$, a wide gap in the luminosity function appears between VLMs at $\log L/L_\odot \approx -3$ and very old, cold BDs at $\log L/L_\odot \approx -6$, but the luminosity function continues to increase even at very low luminosities.

The IMF index values derived above all yield an increasing number of objects for decreasing mass at and just below the main sequence boundary. If α for ρ Oph is as steep as 2.35, and is typical for the rest of the galaxy, then brown dwarfs down to $\sim$0.01 solar masses contribute a mass density that would be comparable to that of main-sequence stars in the galaxy

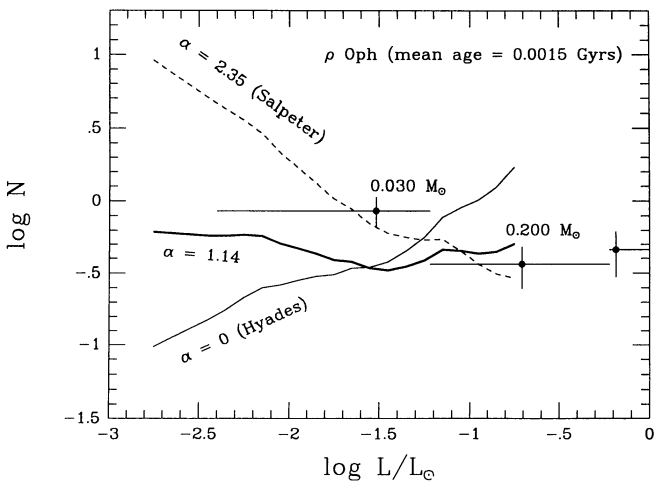

FIG. 12a

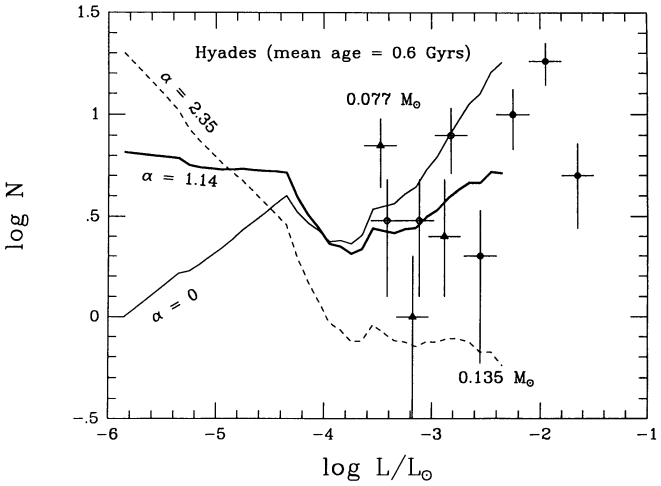

FIG. 12b

FIG. 12.—(*a*) Luminosity functions for ρ Oph, compared with data from Comeron et al. (1992); see text for explanation. (*b*) Luminosity functions for Hyades, compared with data from Leggett & Hawkins (1988, 1989) and Bryja et al. (1992); see text for explanation.

(Stevenson 1978). However, a survey of the 8 pc neighborhood around the Sun by Henry (1991) for low-mass binary companions yielded an IMF α of 0.75 for objects down to the main-sequence threshold. Detection of less massive objects is hampered in his survey by the age of objects in the solar neighborhood and, hence, the significant dropoff of luminosity below the main sequence, but an index of 2.35 is clearly inconsistent with his results at and above the main sequence.

Henry (1991) argues that the Hubbard et al. (1990) α value of zero for the Hyades is inconsistent with his determination for the solar neighborhood. With the new data of Bryja et al. (1992), and a redetermination of the Hyades index as being between roughly 0 and 1, the Hyades and solar neighborhood results are now consistent. The significance of such an agreement is clouded by the fact that the Henry (1991) survey focused on binary companions to known M dwarfs; the IMF for free-floating low-mass objects near the Sun is very poorly known.

With the data available, our tentative conclusion is that the IMF at the main-sequence edge is less steep than the Salpeter mass function, but does imply an increasing population of objects for decreasing mass. ρ Oph may have a steeper IMF than either the Hyades or the solar neighborhood, which is conceivably connected with its very high star formation efficiency (Zinnecker, McCaughrean, & Wilking 1992). Determination of the Pleiades IMF at and below the main sequence boundary is obviously of high interest in this regard, but the data appear too uncertain and contradictory to permit such a determination at this time.

5. ZERO-METALLICITY MODELS

Below we present models for a gas of pure hydrogen and helium, using opacity data from Lenzuni et al. (1991). When comparison is made with the solar metallicity objects of the previous sections, the models demonstrate the important effect metals have on the evolution curves of mass and luminosity, and particularly on the threshold mass of the main-sequence boundary. A later paper (Saumon et al. 1993), will focus on the effect of gray versus nongray atmospheres on brown dwarf properties in the metal-free limit.

The metal-free models correspond to Population III objects, for which searches have to date been fruitless at all masses.

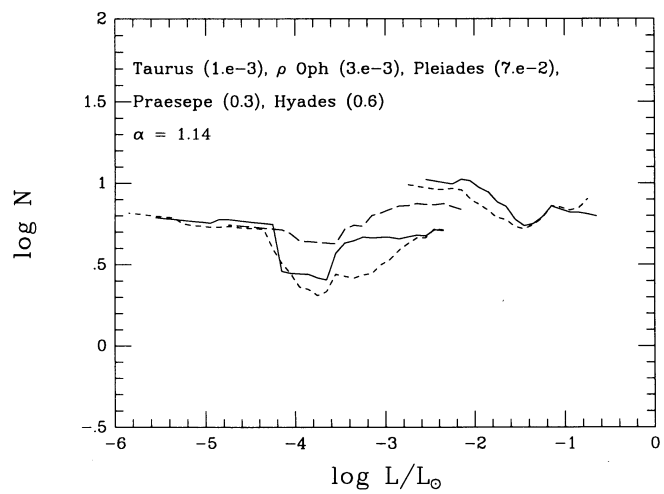

FIG. 13.—Same as Fig. 11, but for α = 1.14

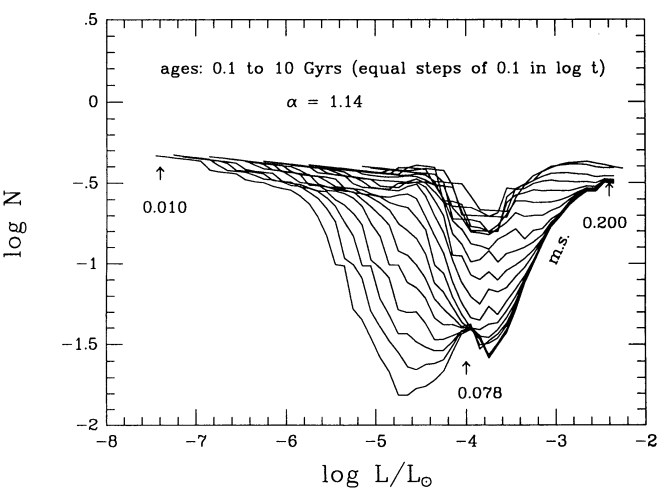

FIG. 14.—Same as Fig. 8, but for α = 1.14

High-velocity, metal-poor subdwarfs in the solar neighborhood are seen at masses down to 0.1 solar masses, based on observations of Monet et al. (1992), and models of D'Antona (1987). These assume a metallicity of 0.01 times solar or Population II. An interesting issue is whether the use of pure hydrogen-helium models significantly changes the interpretation of the observations of Monet et al. (1992), in terms of the masses. Determining the degree of sensitivity of model properties at low metallicity is required for determining the IMF of halo subdwarfs from observations.

Interpretation of surveys of field halo populations (Richer & Fahlman 1992) are hampered by the fair range of metallicity expected for such objects. The halo field star results down to 0.14 solar masses are consistent with a Salpeter mass function (Richer & Fahlman 1992); extrapolating downward in mass would allow low-mass brown dwarfs to dominate the dark matter content of the galaxy (Burrows & Liebert 1993). Thus, while Population III objects may be absent from the halo, use of our metal-free models provides an important sensitivity test in the interpretation of metal-poor subdwarfs, using the most up-to-date continuum opacities available.

Our zero-metallicity atmosphere models include all known continuum sources of opacity of importance contributed by H_2, H_2^+, H^-, He^-, He, H, e^-, and He^+ as recently updated by Lenzuni et al. (1991). In the pressure and temperature regime of interest for low-mass stars and brown dwarfs, the dominant sources of opacity are H^-, bound-free, and free-free, pressure-induced H_2 absorption, and Rayleigh scattering from H_2 and H. The new opacities tabulated by Lenzuni et al. (1991), include a substantial improvement in the pressure-induced H_2 absorption contribution, increasing the monochromatic opacity of the H_2-H_2 contribution by a factor of 3 over the work of Patch (1971) and the H_2-He contribution by up to a factor of 30 over that of Linsky (1969). Note that these are true zero-metallicity opacities, as opposed to the Tsuji (1971) opacities used in the low-opacity model "E" of BHL, which retain contributions from some metals and, therefore, overestimate the H^- contribution to the total opacity.

A sequence of gray models with a gravity typical of evolved brown dwarfs and of the lower main sequence is shown in Figure 15. For each model, the top of the convection zone is indicated by a dot. The convection zone is found to rise in the atmosphere as T_e increases, from $\log \tau = 2.02$ for $T_e = 1000$ K to $\log \tau = -2.20$ for $T_e = 4500$ K, where τ is the Rosseland mean optical depth. This is due to the monotonic increase of the Rosseland mean opacity, κ_R, with T and the smaller values of the adiabatic gradient ∇_{ad} found in the region of partial dissociation of H_2. For comparison, the same sequence of models, but with $Z = Z_\odot$, is shown in Figure 16. The higher opacity of a mixture containing a solar abundance of metals reduces the atmospheric pressure dramatically at the onset of adiabaticity. Again, the top of the convection zone moves upward as T_e increases, going from $\log \tau = 1.41$ for $T_e = 1000$ K to a minimum of $\log \tau = -1.80$ for the $T_e = 4000$ K model. At higher temperatures, the convection zone retreats back to deeper layers as ∇_{ad} increases due to nearly complete dissociation of H_2.

The evolution of very low mass stars and brown dwarfs under a low-opacity atmospheric boundary condition has been discussed in some detail in BHL (model E sequence). The new zero-metallicity sequences presented here are much more detailed and include a much improved treatment of the atmospheric boundary condition.

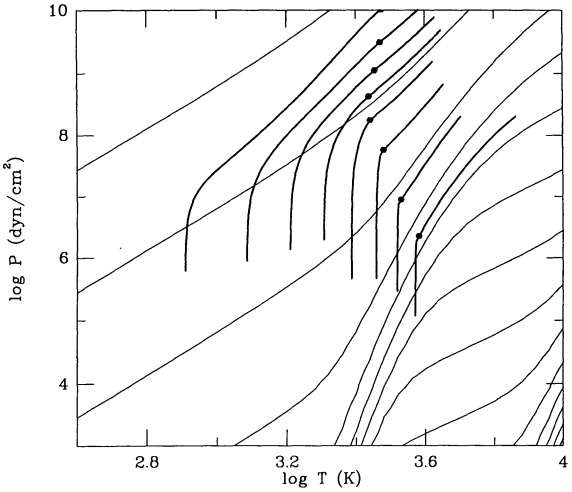

FIG. 15.—$P(T)$ profiles for zero-metallicity gray atmospheres on the same entropy background as Fig. 1. Effective temperature increases from 1000 K (*left*) to 4500 K (*right*) by steps of 500 K. All models have $\log g = 5.5$. A dot indicates the locations of the top of the convection zone that rises in the atmosphere as T_e increases.

The evolution of the zero-metallicity case is homologous to that of the solar metallicity models discussed in § 3. We refer to the zero-metallicity model with $Y_\alpha = 0.25$ and $\alpha = 1.0$ as model Z. Figure 17 depicts the evolution of the luminosity with time for various masses and shows that $Z = 0$ models evolve faster in the sense that every phase of the evolution (deuterium burning, settling on the main sequence, split between stars and brown dwarfs) occurs about a factor of 10 earlier in time than in the solar metallicity case (Fig. 3). This is a direct consequence of the lower atmospheric opacities. For *fixed* T_e and g, the lower κ_R forces the top of the convection zone farther down into the atmosphere to higher pressures, where the specific entropy is *lower*. Since convection is very nearly adiabatic, the entropy of the interior is fixed by the P and T values at the top of the convection zone. Conversely, for models with a fixed *mass* and interior entropy (which determine the structure of a model), the $Z = 0$ model will have nearly the same radius, but

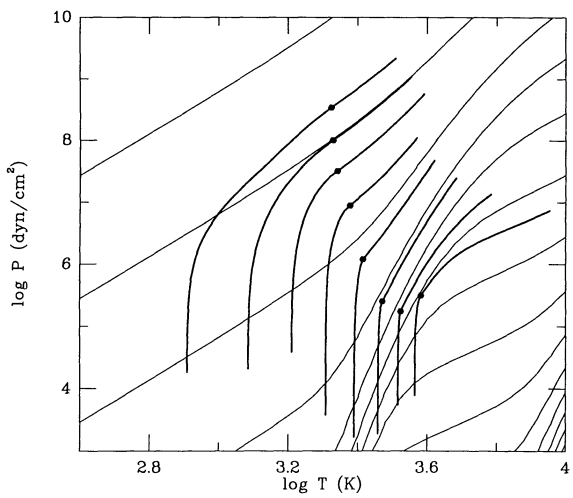

FIG. 16.—Same as Fig. 15, but for solar metallicity models. The convection zone starts to retreat in the atmosphere for $T_e > 4000$ K.

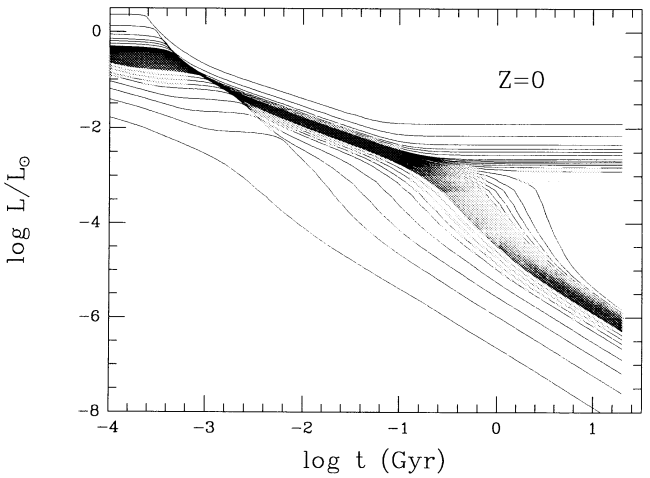

FIG. 17.—Same as Fig. 3, but for Population III

a higher T_e. This results in a higher luminosity and faster evolution.

Another consequence of lower atmospheric opacities is the increase of the minimum mass for hydrogen burning on the main sequence. For models that reach a stable configuration on the main sequence, the higher luminosity of the $Z = 0$ case requires more vigorous nuclear burning to maintain the equilibrium. This can be achieved only for higher mass stars. As shown in Figure 2 and Table 1, the dependence of T_e and L at the edge of the main sequence on Z is very strong. We emphasize the importance of accurate opacities for the determination of the location of the edge of the main sequence. In a similar calculation, D'Antona (1987), computed a value of $M = 0.115$ $M_\odot$ for the zero-metallicity minimum main sequence mass based on the opacity table of Cox & Tabor (1976). These opacities do not include the contributions of H_2 and of molecular ions and thereby underestimate the opacity at low temperatures ($T_e < 3000$ K) and raise the estimate of the mass at the edge of the $Z = 0$ main sequence.

Due to their higher pre–main-sequence luminosity, $Z = 0$ stars *of a given mass* settle onto the main sequence at a lower specific entropy than their solar metallicity homologues. As a consequence, they have smaller radii, higher central densities,

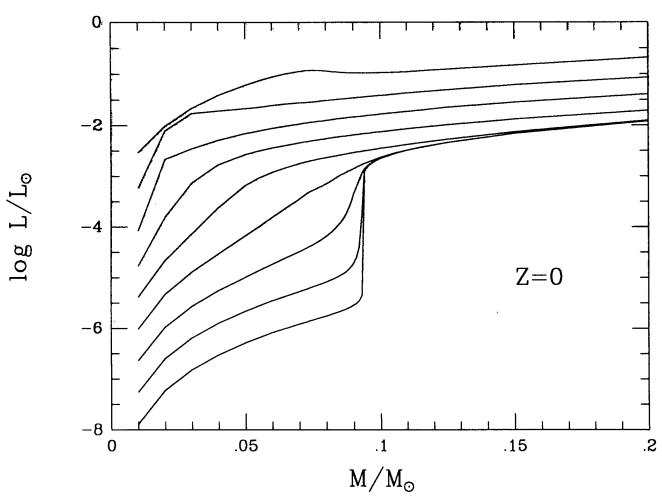

FIG. 18.—Same as Fig. 6, but for Population III

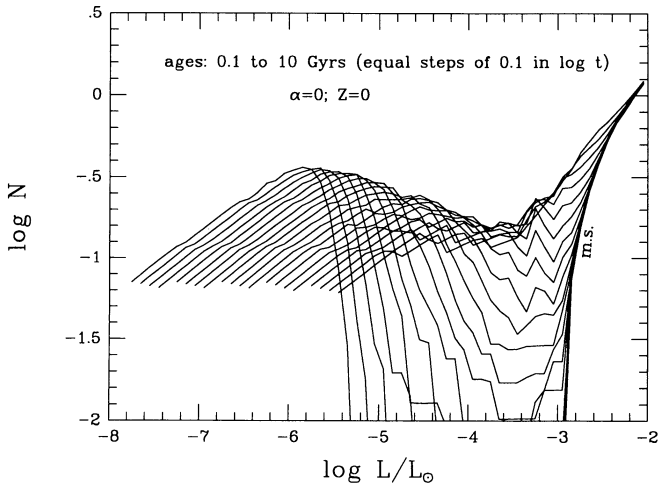

FIG. 19.—Same as Fig. 8, but for Population III

and lower central temperatures. For zero metallicity, T_e is generally higher on the VLM branch, but lower on the old brown dwarf branch, than in the corresponding solar case. These trends follow directly and naturally from the lower opacities at $Z = 0$ and bound extreme subdwarf behavior.

Figures 18 and 19 are the model Z versions of Figures 6 and 8. Note that the gaps in the luminosity functions in Figure 19 are much wider and deeper than in the solar case. Both Figures 18 and 19 reflect the more abrupt separation of the VLM and brown dwarf families at zero metallicity. Table 3 summarizes some of the important characteristics, at a few representative times, of model Z objects. If there is a significant population of halo brown dwarfs, their properties should be bounded by those of model Z. Therefore, since halo objects are expected to be older and of lower metallicity than disk objects, we should expect halo brown dwarfs to be dimmer and colder than their brethren in the disk.

6. COMPARISON WITH OTHER MODELS

Figures 20 and 21 compare our solar and zero-metallicity models with other recent published results of Stringfellow

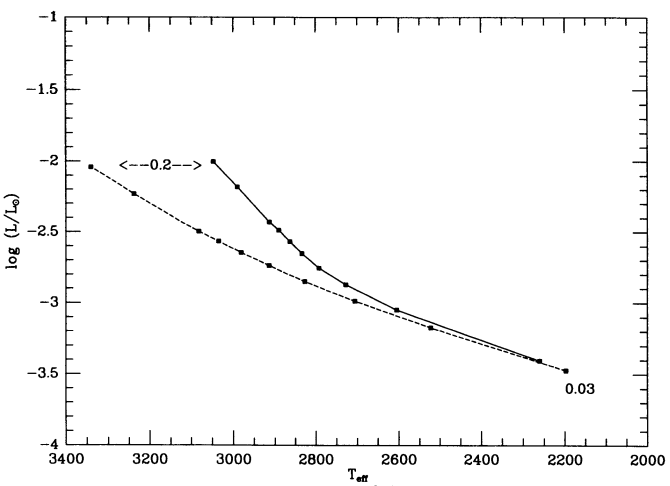

FIG. 20.—Luminosity vs. effective temperature for solar metallicity objects at 7×10^7 yr. The solid curve is from Stringfellow (1991), and the dashed curve is computed using the model described herein. The mass range in each case is 0.2–0.03 solar masses.

TABLE 3

MODEL Z

$M/M_\odot$	Age	T_e	$L/L_\odot$	R	T_c	ρ_c	S	L_n/L
	10^9 yrs	K		10^9 cm	10^6 K	g/cm^3	k_B/baryon	
0.200	0.003	4480.	9.000E-02	34.60	2.960	12.8	15.09	0.000
	0.070	4240.	1.340E-02	14.90	6.320	159.0	12.91	0.648
	0.600	4240.	1.220E-02	14.30	6.560	181.0	12.79	1.000
0.150	0.003	4320.	6.430E-02	31.50	2.420	12.5	14.64	0.000
	0.070	4150.	8.450E-03	12.40	5.420	205.0	12.15	0.426
	0.600	4130.	6.970E-03	11.30	5.780	268.0	11.89	1.000
0.125	0.003	4230.	5.220E-02	29.50	2.140	12.5	14.33	0.000
	0.070	4080.	6.320E-03	11.00	4.860	238.0	11.65	0.280
	0.600	4050.	4.620E-03	9.59	5.280	362.0	11.21	1.000
0.115	0.003	4200.	4.750E-02	28.60	2.030	12.6	14.19	0.000
	0.070	4050.	5.540E-03	10.50	4.590	254.0	11.43	0.221
	0.600	4010.	3.730E-03	8.82	5.010	428.0	10.86	1.000
0.110	0.003	4190.	4.510E-02	28.10	1.970	12.8	14.12	0.000
	0.070	4040.	5.170E-03	10.20	4.370	265.0	11.31	0.190
	0.600	3980.	3.270E-03	8.38	4.770	480.0	10.65	1.000
0.105	0.003	4170.	4.290E-02	27.60	1.910	12.8	14.04	0.000
	0.070	4020.	4.800E-03	9.95	4.260	272.0	11.19	0.162
	0.600	3930.	2.800E-03	7.92	4.630	537.0	10.40	0.999
	10.000	3930.	2.800E-03	7.92	4.630	538.0	10.40	1.000
0.100	0.003	4150.	4.070E-02	27.10	1.850	12.8	13.96	0.000
	0.070	4000.	4.440E-03	9.67	4.150	278.0	11.05	0.134
	0.600	3870.	2.270E-03	7.36	4.450	630.0	10.07	1.000
0.098	0.003	4140.	3.990E-02	27.00	1.820	12.8	13.93	0.000
	0.070	3990.	4.300E-03	9.56	4.010	285.0	10.99	0.122
	0.600	3830.	2.030E-03	7.11	4.220	690.0	9.90	0.983
	10.000	3830.	2.010E-03	7.09	4.220	696.0	9.89	1.000
0.096	0.003	4140.	3.900E-02	26.80	1.800	12.8	13.89	0.000
	0.070	3980.	4.160E-03	9.45	3.890	291.0	10.94	0.112
	0.600	3780.	1.760E-03	6.82	3.980	769.0	9.69	0.970
	10.000	3770.	1.720E-03	6.77	3.970	787.0	9.66	1.000
0.094	0.003	4130.	3.820E-02	26.60	1.770	12.8	13.86	0.000
	0.070	3970.	4.020E-03	9.34	3.850	293.0	10.88	0.103
	0.600	3700.	1.490E-03	6.53	3.820	853.0	9.46	0.915
	10.000	3630.	1.260E-03	6.25	3.680	967.0	9.24	1.000
0.092	0.003	4120.	3.740E-02	26.40	1.740	12.8	13.82	0.000
	0.070	3960.	3.890E-03	9.23	3.790	296.0	10.82	0.092
	0.600	3590.	1.180E-03	6.18	3.530	976.0	9.15	0.795
	10.000	957.	3.480E-06	4.73	0.976	2150.0	6.41	0.088
	20.000	748.	1.270E-06	4.68	0.825	2210.0	6.10	0.068
0.090	0.003	4110.	3.660E-02	26.20	1.710	12.7	13.79	0.000
	0.070	3940.	3.750E-03	9.12	3.730	299.0	10.76	0.083
	0.600	3420.	8.780E-04	5.88	3.190	1100.0	8.82	0.613
	10.000	911.	2.890E-06	4.74	0.934	2070.0	6.35	0.063
	20.000	721.	1.110E-06	4.70	0.798	2130.0	6.06	0.049
0.088	0.003	4110.	3.580E-02	26.00	1.690	12.7	13.75	0.000
	0.070	3930.	3.610E-03	9.01	3.660	303.0	10.69	0.074
	0.600	3210.	6.310E-04	5.65	2.820	1210.0	8.51	0.411
	10.000	880.	2.530E-06	4.77	0.894	1990.0	6.32	0.044
	20.000	702.	1.010E-06	4.72	0.767	2050.0	6.04	0.035
0.086	0.003	4100.	3.500E-02	25.80	1.660	12.7	13.72	0.000
	0.070	3920.	3.480E-03	8.90	3.520	309.0	10.63	0.065
	0.600	3080.	5.060E-04	5.51	2.440	1280.0	8.26	0.241
	10.000	855.	2.290E-06	4.79	0.838	1920.0	6.29	0.032
	20.000	685.	9.210E-07	4.75	0.721	1970.0	6.02	0.025
0.084	0.003	4090.	3.420E-02	25.60	1.630	12.6	13.68	0.000
	0.070	3910.	3.350E-03	8.79	3.430	313.0	10.56	0.057
	0.600	2840.	3.570E-04	5.42	2.180	1310.0	8.07	0.166
	10.000	834.	2.090E-06	4.82	0.801	1840.0	6.27	0.023
	20.000	669.	8.480E-07	4.77	0.691	1890.0	6.00	0.018
0.082	0.003	4080.	3.350E-02	25.50	1.610	12.5	13.65	0.000
	0.070	3890.	3.220E-03	8.68	3.380	315.0	10.49	0.050
	0.600	2680.	2.750E-04	5.37	2.020	1310.0	7.92	0.111
	10.000	814.	1.920E-06	4.84	0.785	1760.0	6.25	0.016
	20.000	654.	7.830E-07	4.80	0.679	1810.0	5.98	0.013

TABLE 3—*Continued*

$M/M_\odot$	Age	T_e	$L/L_\odot$	R	T_c	ρ_c	S	L_n/L
	10^9 yrs	K		10^9 cm	10^6 K	g/cm^3	k_B/baryon	
0.080	0.003	4070.	3.290E-02	25.30	1.570	12.4	13.61	0.000
	0.070	3880.	3.090E-03	8.57	3.310	318.0	10.42	0.043
	0.600	2540.	2.210E-04	5.34	1.880	1290.0	7.81	0.074
	10.000	797.	1.780E-06	4.87	0.760	1690.0	6.23	0.011
	20.000	641.	7.350E-07	4.83	0.659	1730.0	5.97	0.009
0.075	0.003	4050.	3.080E-02	24.80	1.510	12.5	13.51	0.000
	0.070	3830.	2.770E-03	8.30	3.010	329.0	10.23	0.028
	0.600	2220.	1.290E-04	5.34	1.530	1210.0	7.62	0.030
	10.000	756.	1.480E-06	4.94	0.671	1500.0	6.19	0.004
	20.000	608.	6.100E-07	4.90	0.583	1540.0	5.93	0.003
0.070	0.003	4030.	2.890E-02	24.20	1.460	12.3	13.42	0.000
	0.070	3780.	2.450E-03	8.03	2.820	334.0	10.03	0.017
	0.600	2010.	8.730E-05	5.38	1.370	1090.0	7.49	0.011
	10.000	715.	1.230E-06	5.02	0.627	1330.0	6.15	0.002
	20.000	576.	5.070E-07	4.98	0.546	1360.0	5.89	0.001
0.065	0.003	4010.	2.770E-02	24.00	1.340	11.5	13.34	0.000
	0.070	3710.	2.130E-03	7.76	2.520	344.0	9.82	0.009
	0.600	1820.	6.040E-05	5.43	1.150	978.0	7.39	0.003
	10.000	675.	1.010E-06	5.10	0.550	1170.0	6.11	0.000
	20.000	543.	4.160E-07	5.06	0.479	1190.0	5.86	0.000
0.060	0.003	3980.	2.640E-02	23.70	1.250	11.1	13.24	0.000
	0.070	3620.	1.800E-03	7.51	2.260	347.0	9.57	0.004
	0.600	1660.	4.340E-05	5.51	1.010	859.0	7.30	0.001
	10.000	637.	8.260E-07	5.20	0.501	1010.0	6.07	0.000
	20.000	513.	3.420E-07	5.16	0.438	1030.0	5.82	0.000
0.055	0.003	3960.	2.440E-02	23.10	1.170	11.0	13.13	0.000
	0.070	3490.	1.460E-03	7.26	1.940	348.0	9.31	0.002
	0.600	1530.	3.170E-05	5.59	0.860	746.0	7.23	0.000
	10.000	596.	6.600E-07	5.30	0.439	870.0	6.03	0.000
	20.000	480.	2.740E-07	5.26	0.385	888.0	5.79	0.000
0.050	0.003	3930.	2.310E-02	22.70	1.080	10.5	13.02	0.000
	0.070	3310.	1.120E-03	7.05	1.610	344.0	9.03	0.000
	0.600	1400.	2.310E-05	5.69	0.712	637.0	7.15	0.000
	10.000	558.	5.260E-07	5.41	0.381	736.0	5.99	0.000
	20.000	449.	2.180E-07	5.37	0.334	751.0	5.75	0.000
0.040	0.003	3870.	2.160E-02	22.70	0.868	8.3	12.87	0.002
	0.070	2780.	5.070E-04	6.76	1.030	304.0	8.41	0.000
	0.600	1150.	1.170E-05	5.93	0.497	440.0	7.00	0.000
	10.000	474.	3.010E-07	5.66	0.285	500.0	5.91	0.000
	20.000	382.	1.260E-07	5.62	0.252	509.0	5.68	0.000
0.030	0.003	3790.	1.790E-02	21.60	0.687	6.9	12.56	0.777
	0.070	2020.	1.430E-04	6.77	0.617	217.0	7.91	0.000
	0.600	927.	5.370E-06	6.25	0.342	273.0	6.86	0.000
	10.000	390.	1.540E-07	5.99	0.203	306.0	5.83	0.000
	20.000	314.	6.410E-08	5.95	0.181	311.0	5.61	0.000
0.020	0.003	3640.	7.940E-03	15.50	0.576	11.9	11.35	0.917
	0.070	1420.	3.760E-05	7.08	0.338	120.0	7.59	0.000
	0.600	704.	2.020E-06	6.65	0.202	142.0	6.68	0.000
	10.000	297.	5.970E-08	6.41	0.124	157.0	5.72	0.000
	20.000	239.	2.480E-08	6.37	0.112	159.0	5.52	0.000
0.010	0.003	2540.	6.430E-04	9.15	0.265	25.8	8.84	0.000
	0.070	877.	6.300E-06	7.56	0.142	43.8	7.25	0.000
	0.600	459.	4.300E-07	7.20	0.092	49.7	6.46	0.000
	10.000	194.	1.280E-08	6.97	0.060	54.1	5.62	0.000

(1991) and D'Antona (1987). In Figure 20 we have constructed an H-R diagram for solar metallicity objects at 7×10^7 yr, the upper end of the Pleiades age estimates, and compared this with the curve generated by Stringfellow (1991) for the same conditions. Above 2800 K there are significant differences between the two.

We attribute this discrepancy to two major differences between our respective models: (1) the treatment of the surface boundary condition and (2) the interior equation of state. Stringfellow (1986) obtains a surface pressure at $\tau = 1$ by solving $P = g/\kappa_R$. This approximate surface boundary condition rests on the assumption that the atmosphere is in radiative equilibrium for $\tau < 1$, which we find is *not* the case for gray models with $T_e \geq 2400$ K in which the convection zone reaches into the optically thin part of the atmosphere. In view of the demonstrated importance of solving the radiative transfer problem for the hotter atmospheres to obtain reliable surface boundary conditions for the interior models (§ 2), we expect

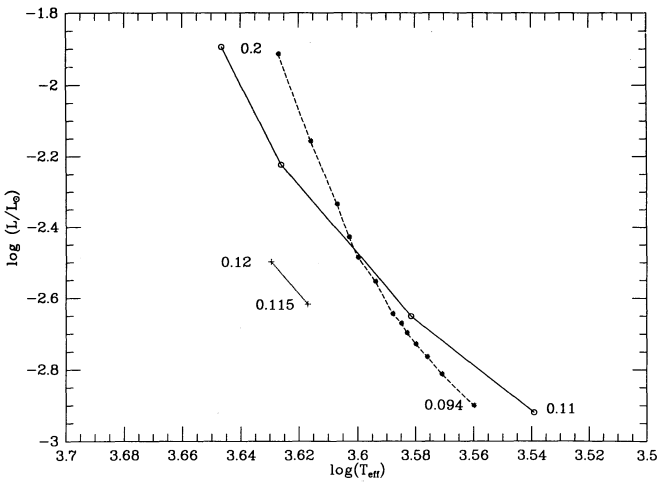

FIG. 21.—Luminosity vs. effective temperature for models of low and zero metallicity. The zero-metallicity models described in the text are plotted as asterisks, the zero metallicity models of D'Antona (1987) are plotted as pluses, and D'Antona's 10^{-4} solar metallicity models are plotted as open circles. The masses for the open circles are (in solar masses), 0.2, 0.15, 0.12, and 0.11; for the asterisks, the run is 0.2, 0.15, 0.125, 0.115, 0.110, 0.105, 0.1, 0.099, 0.098, 0.097, 0.096, 0.095, and 0.094.

Stringfellow's simple approach to deviate from our results at relatively high T_e.

Stringfellow uses the Eggleton, Faulkner, & Flannery (1973) equation of state which ignores Coulomb corrections in the dense, fully ionized regime. These corrections are important for the description of the thermal structure of brown dwarfs and will also affect the mechanical structure of young and relatively massive objects which are partially degenerate. Ignoring the Coulomb corrections to the pressure and entropy, which are negative, leads to an overestimate of the pressure and to larger radii, as seen in Figure 20. At lower effective temperatures and lower masses, where brown dwarfs are more degenerate, both of these effects decrease in importance as can be seen by the excellent agreement between the 0.03 $M_\odot$ models in Figure 20.

The implications of the new models for the Pleiades cluster depend to a large extent on the resolution of current disagreements regarding the observations. In general, our curve would fit the bulk of the low-mass star data for the Pleiades somewhat better than Stringfellow's curve. However, because of the problems with the interpretation of the data (described in Stringfellow 1991) we choose not to explore this issue at the present time.

Figure 21 is a similar plot comparing our zero-metallicity models against those of D'Antona (1987) for $Z = 10^{-4}$ and $Z = 0$, for main-sequence objects only. Here our zero-metallicity curve runs closely along the D'Antona 10^{-4} model, but with a steeper slope. Much of the shift between the zero-metallicity models lies in the larger values of hydrogen-helium opacity in our case. Another effect at the high end is D'Antona's use of a modified Eddington $T(\tau)$ relationship in computing model atmospheres. The result of this is an underestimate of the interior entropy which tends to slide the D'Antona models to the left of ours. At lower effective temperature the modified Eddington profile is perfectly adequate for deriving the entropy, and opacities due to molecules are becoming important in the $Z = 10^{-4}$ models of D'Antona. Both of these effects shift the bottom of the D'Antona curves rightward in the diagram relative to ours, and cause our $Z = 0$ model to have a steeper slope than the D'Antona $Z = 10^{-4}$ models.

The implications of our new zero-metallicity models lie in the interpretation of observations such as those of Monet et al. (1992). Subdwarfs plotted on an H-R diagram would lie closer to our zero-metallicity line than to the D'Antona (1987) zero-metallicity models. It is possible that some of the subdwarfs in the Monet et al. survey have lower metallicity than estimated previously. If the metallicities of these objects are fixed by spectra, then our curve would imply a lower mass for a given object than would the D'Antona curve.

7. CONCLUSION

There are now many brown dwarf candidates in the field and in clusters (Burrows & Liebert 1993). As a consequence, the observational study of the edge of the hydrogen main sequence is advancing rapidly. In this paper, we provided a new and dense grid of brown dwarf and M dwarf stellar models between 0.01 and 0.2 $M_\odot$. Since young substellar objects are hot and bright and are selected for in cluster searches, we focused on their early ($\geq 10^6$ yr) evolution. Because deuterium burning ($\leq 10^7$ yr) is particularly important during a brown dwarf's early contraction phase, its consequences were given special attention. Furthermore, we solved the full atmosphere problem in both the radiance and outer convective regions to avoid errors that can be introduced in the outer thermal structure and in the effective temperatures when the Eddington ($\tau = 2/3$) approximation is used. Such errors can amount to hundreds of kelvins. We also generated a variety of luminosity functions, compared them to data for ρ Oph and the Hyades, and identified diagnostic features in luminosity functions near and below the main-sequence edge.

Because of the continuing interest in brown dwarfs as possible halo constituents, we calculated zero-metallicity (Population III) brown dwarf and VLM models. The combination of improved physics and opacities over earlier models (Fig. 21) implies a possible need to reinterpret the metallicity or masses of recently observed subdwarf populations. We noted that, as a consequence of the new H_2/He opacities of Lenzuni et al. (1991), the main sequence edge is below 0.094 $M_\odot$ for any metallicity and for helium fractions above 0.22. With our new models, X and Z, we have built on the work of BHL and hope to provide the observers with a more extensive theory both at early ages and over a broad mass range. As observers continue to push their techniques to detect fainter objects, the models presented here can be used to deepen our understanding of the abundance and properties of the lowest mass components of the Galactic disk.

The authors would like to thank G. Rieke, T. Henry, D. Kirpatrick, S. Leggett, P. Bergeron, and P. Lenzuni for useful conversations, and advice. A. B. acknowledges the support of the NSF and NASA through grants AST89-14346 and NAGW-2145, respectively, as do J. I. L. and W. B. H. for support under NSF grant AST89-10780. D. S. gratefully acknowledges a Postdoctoral Fellowship from the Natural Sciences and Engineering Research Council of Canada.

REFERENCES

Bergeron, P., Wesemael, F., & Fontaine, G. 1990, ApJ, 367, 253
Bryja, C., Jones, T. J., Humphreys, R. M., Lawrence, G., Pennington, R. L., & Zumach, W. 1992, ApJ, 388, L23
Burrows, A., Hubbard, W. B., & Lunine, J. I. 1989, ApJ, 345, 939 (BHL)
Burrows, A., & Liebert, J. 1993, Rev. Mod. Phys., in press
Comeron, F., Rieke, G. H., Burrows, A., & Rieke, M. J. 1993, preprint
Cox, A. N., & Tabor, T. E. 1976, ApJS, 31, 271
D'Antona, F. 1987, ApJ, 320, 653
D'Antona, F., & Mazzitelli, I. 1985, ApJ, 296, 502
Dorman, B., Nelson, L. A., & Chau, W. Y. 1989, ApJ, 342, 1003
Eggleton, P. P., Faulkner, J., & Flannery, B. P. 1973, A&A, 23, 325
Henry, T. 1991, Ph.D. thesis, Univ. of Arizona, Tucson
Henry, T. J., & McCarthy, D. W., Jr. 1990, ApJ, 350, 334
Hubbard, W. B., Burrows, A., & Lunine, J. I. 1990, ApJ, 358, L53
Leggett, S. K., & Hawkins, M. R. S. 1988, MNRAS, 234, 1065
———. 1989, MNRAS, 238, 145
Lenzuni, P., Chernoff, D., & Salpeter, E. E. 1991, ApJS, 76, 759
Linsky, J. L. 1969, ApJ, 156, 989
Lunine, J. I., Hubbard, W. B., Burrows, A., Wang, Y. P., & Garlow, K. 1989, ApJ, 338, 314
Monet, D. G., Dahn, C. C., Vrba, F. J., Harris, H. C., Pier, J. R., Luginbuhl, C. B., & Ables, H. D. 1992, ApJ, 103, 638
Nelson, L., Rappaport, S., & Joss, P. 1985, Nature, 316, 42
———. 1993, ApJ, in press
Patch, R. W. 1971, J. Quant. Spectrosc. Rad. Transf., 11, 131
Richer, H. B., & Fahlman, G. G. 1992, Nature, in press
Salpeter, E. E. 1955, ApJ, 121, 161
Saumon, D., Lunine, J. I., Hubbard, W. B., & Burrows, A. 1993, in preparation
Simons, D. A., & Becklin, E. E. 1992, ApJ, 390, 431
Stevenson, D. J. 1978, Proc. Astron. Soc. Australia, 3, 227
Stringfellow, G. S. 1986, in Astrophysics of Brown Dwarfs, ed. M. C. Kafatos, R. S. Harrington, & S. P. Maran (Cambridge: Cambridge Univ. Press), 190
———. 1991, ApJ, 375, L21
Tsuji, T. 1971, PASJ, 23, 553
Zinnecker, H., McCaughrean, M. J., & Wilking, B. A. 1992, in Protostars and Planets III, ed. E. Levy & J. Lunine (Tucson: Univ. of Arizona Press), in press